Distinct Magnetic Gaps between Antiferromagnetic and Ferromagnetic Orders Driven by Surface Defects in the Topological Magnet $MnBi_2Te_4$

Hengxin Tan and Binghai Yan
Department of Condensed Matter Physics, Weizmann Institute of Science, Rehovot 7610001, Israel

(Received 27 July 2022; accepted 3 March 2023; published 24 March 2023)

Many experiments observed a metallic behavior at zero magnetic fields (antiferromagnetic phase, AFM) in $MnBi_2Te_4$ thin film transport, which coincides with gapless surface states observed by angle-resolved photoemission spectroscopy, while it can become a Chern insulator at field larger than 6 T (ferromagnetic phase, FM). Thus, the zero-field surface magnetism was once speculated to be different from the bulk AFM phase. However, recent magnetic force microscopy refutes this assumption by detecting persistent AFM order on the surface. In this Letter, we propose a mechanism related to surface defects that can rationalize these contradicting observations in different experiments. We find that co-antisites (exchanging Mn and Bi atoms in the surface van der Waals layer) can strongly suppress the magnetic gap down to several meV in the AFM phase without violating the magnetic order but preserve the magnetic gap in the FM phase. The different gap sizes between AFM and FM phases are caused by the exchange interaction cancellation or collaboration of the top two van der Waals layers manifested by defect-induced surface charge redistribution among the top two van der Waals layers. This theory can be validated by the position- and field-dependent gap in future surface spectroscopy measurements. Our work suggests suppressing related defects in samples to realize the quantum anomalous Hall insulator or axion insulator at zero fields.

DOI: 10.1103/PhysRevLett.130.126702

Introduction.—Magnetic topological insulators (TIs) have long been sought for the realization of the quantized anomalous Hall effect (QAHE) [1] and axion insulator (AI) [2–4]. Recent discovery of an intrinsic magnetic TI, $MnBi_2Te_4$ [5–8], sparks extensive research interest in realizing QAH and AI [9–13], and leads to discovering a general family of magnetic TIs, $MnBi_2Te_4(Bi_2Te_3)_n$ [14–29]. $MnBi_2Te_4$ is a van der Waals (vdW)-type layered material. Its ground state exhibits the *A*-type antiferromagnetic (AFM) order where each vdW layer shows ferromagnetic (FM) coupling with the easy axis orienting out-of-plane while adjacent layers couple in an AFM way. $MnBi_2Te_4$ was predicted to be a magnetic TI in which the Dirac states open a magnetic gap on the vdW surface [6–8,30–33], which is promising for the realization of QAHE and AI.

While some experiments observed gapped surface states [6,34–37], many other angle-resolved photoemission spectroscopy (ARPES) experiments [38–43] observed gapless surface states contradicting theoretical predictions [6–8,30–33]. Thus, it was once speculated that the original surface FM order was broken to rationalize the absence of a surface magnetic gap [24,38,41]. However, the following magnetic force microscopy [44] and ARPES [45] experiments revealed a robust *A*-type AFM order on the surface.

In transport experiments, realizing gapped topological surface states remains a major challenge [13,19,46], although the QAHE [9] and AI [11] states were reported in $MnBi_2Te_4$ thin films. Except for this recent experimental realization of QAHE in a five-layer $MnBi_2Te_4$ film [9], most films with an odd number of $MnBi_2Te_4$ layers, which were expected to exhibit QAHE, commonly show non-quantized Hall resistance at zero fields. However, the same film presents a quantized Hall resistance under high magnetic fields > 6 T when the film is polarized to the FM phase [9–11,47–50]. That is to say, the AFM phase exhibits a small (or zero) gap while the FM phase exhibits a finite gap in the same thin film, although calculations predict comparable magnetic gaps for both phases (see our calculations below).

To reconcile the above controversial observations in $MnBi_2Te_4$, a potential mechanism should fulfill at least three conditions. (i) It can explain the gapless or nearly gapless surface states to account for ARPES and zero-field transport experiments. (ii) It should respect the *A*-type AFM order on the surface and bulk region at zero fields. (iii) It can provide a sizable energy gap on the surface in the FM phase.

Because experiments revealed many defects such as antisites in samples [35,51–55], the influence of defects or surface disorders on the magnetic gap has been actively investigated recently [32,35,53,56–61]. Most of these works aim to rationalize the gapless nature of the AFM phase by fulfilling conditions (i)–(ii) but not (iii). For example, Ref. [60] showed dramatic magnetic gap reduction on the surface under the AFM phase by arguing that the Mn_{Bi} antisite (extra Mn replacing Bi) presents a

magnetic moment antiparallel [51–53] to other Mn moments in the same vdW layer, i.e., magnetism cancellation by Mn_{Bi} antisites. However, as we will show in this Letter, parallel alignment of the Mn_{Bi} moment also strongly suppresses the magnetic gap, contradicting the above scenario.

In this Letter, we find that cation co-antisites Mn_{Bi} and Bi_{Mn} (extra Bi replacing Mn) can resolve puzzles regarding the surface magnetic gap by satisfying all three conditions. These defects push topological surface states, which would distribute dominantly on the first vdW layer and show a sizable magnetic gap (60–70 meV) on the clean surface, partially into the second vdW layer. In the AFM phase, magnetic exchange interactions (with topological surface states) from the first and second layers cancel each other and significantly diminish the magnetic gap to several meV. In the FM phase, however, exchange interactions from the top two layers exhibit no cancellation and thus preserve the magnetic gap. This mechanism requires no reconstruction of surface magnetism at zero fields [condition (ii)]. In addition, we find that the resultant surface magnetic gap is insensitive to the orientation of the Mn_{Bi} magnetic moment. Our results also provide insights to understand gapless surface states of $MnBi_2Te_4(Bi_2Te_3)_n$ ($n = 1, 2$) observed in the AFM phase [21,28] and even in the FM phase [21,22].

Method.—In the following, each $MnBi_2Te_4$ vdW layer is called a septuple layer (SL). All the calculations are performed within density functional theory as implemented in Vienna *ab initio* simulation package [62,63]. The generalized gradient approximation describes the exchange-correlation interaction as parametrized by Perdew-Burke-Ernzerhof [64]. The cutoff energy is 350 eV for the plane wave basis. The Mn d electrons are treated with a Hubbard U of 5 eV. The surface band structures under different surface co-antisites are simulated with slab models of 5-SL thick. The in-plane supercell is examined from 2×2 to 4×4 to investigate the antisite density effect. Three different magnetic configurations are considered, i.e., FM where all magnetic moments are parallel, A-type AFM where the Mn_{Bi} moment is parallelly coupled to other magnetic moments in the same SL, and Ferri-AFM where the Mn_{Bi} moment is antiparallel to other moments in the same SL in the A-type AFM framework [see Supplemental Material [65] for details].

Results.—We start from the configurations of antisites Bi_{Mn} and Mn_{Bi} on the surface of $MnBi_2Te_4$. Previous works [55,66] found that Bi_{Mn} and Mn_{Bi} have relatively low formation energies, confirming the easy existence of these defects. The single cation antisite dramatically changes the surface band dispersion due to charge doping (there is no obviously gapped or gapless Dirac cone, see Supplemental Material [65]), which deviates from experimentally observed band structures that show the clear gapped or gapless Dirac cone [6,34–43]. Besides, band structures of cases with two antisites in two different SLs also do not show the unambiguous Dirac cone [65]. In this Letter, we study neutral defects as formed by the combination of Bi_{Mn} and Mn_{Bi} antisites in the same SL with close distance. Four co-antisite configurations of Bi_{Mn}-Mn_{Bi} in the surface SL are considered, i.e., sNN, sNNN, bNN, and bNNN as defined in Fig. 1. More configurations can be found in the Supplemental Material [65].

We find that the next nearest-neighboring Bi_{Mn}-Mn_{Bi} (sNNN and bNNN in Fig. 1) are more stable in energy (dozens of meV) than the corresponding nearest-neighboring Bi_{Mn}-Mn_{Bi} (sNN and bNN in Fig. 1) under the same magnetic configuration, and the sNNN configuration has the lowest total energy [65]. Under high defect density (in-plane cell size 2×2), total energies of sNNN and bNNN under Ferri-AFM are slightly smaller than those under A-type AFM (within 5 meV). With decreasing the defect density (e.g., in-plane cell size 3×3), total energies of different antisite configurations under Ferri-AFM are slightly larger than those under A-type AFM (within 7 meV). The FM phase always has a higher total energy (comparable to the corresponding AFM phase under high defect density). As we will see [65], band structures and charge densities at the Γ point under Ferri-AFM are very similar to those under A-type AFM. Thus in the following, only results for FM and A-type AFM (which will be further abbreviated as AFM) are presented, and results for Ferri-AFM are shown in the Supplemental Material [65].

Figure 2 shows band structures of surfaces with different co-antisites under AFM and FM (in-plane cell size 3×3).

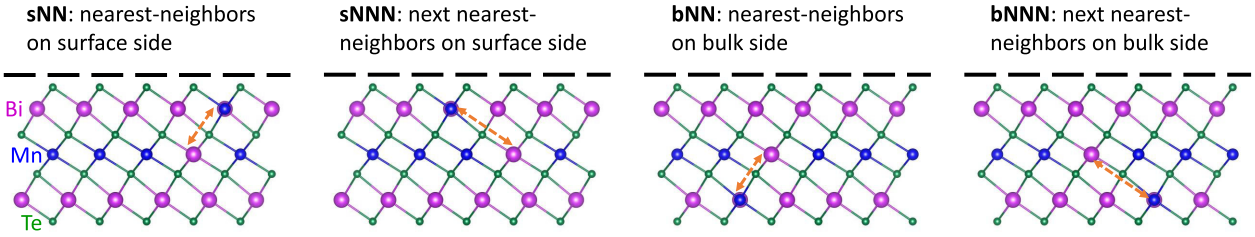

FIG. 1. Cation co-antisite configurations in the surface SL. sNN: nearest-neighboring Mn_{Bi} and Bi_{Mn} on the surface side; sNNN: next nearest-neighboring Mn_{Bi} and Bi_{Mn} on the surface side; bNN: nearest-neighboring Mn_{Bi} and Bi_{Mn} on the bulk side; bNNN: next nearest-neighboring Mn_{Bi} and Bi_{Mn} on the bulk side. For simplicity, only the surface SL is shown where the bold dashed line indicates the surface. The orange vector in each panel connects the antisites Mn_{Bi} and Bi_{Mn}.

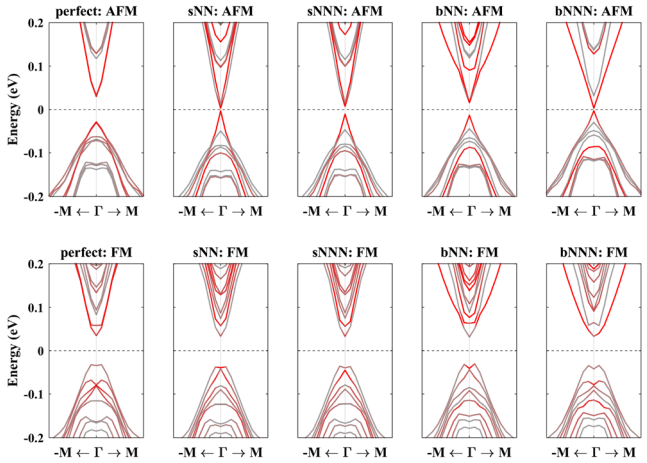

FIG. 2. Band structures of the different co-antisites as shown in Fig. 1. Upper panels: band structures under *A*-type AFM. Lower panels: band structures under FM. For better comparison, the band structures of the perfect surface are also shown (titled *perfect*). The color red stands for the surface SL weight to the bands while the color gray stands for the weight from the rest of the slab. Here we still employ the -*M*-Γ-*M* *k* path of the hexagonal Brillouin zone of the perfect surface, though the surfaces with antisites may no longer have the hexagonal Brillouin zone. The band structures along the -*K*-Γ-*K* line of the hexagonal Brillouin zone share similar band characters [65]. Band gaps are found in Table I.

For the perfect surface, band structures of AFM and FM phases show large gaps (∼60 meV for AFM and ∼69 meV for FM, see Table I). However, when co-antisites appear on the surface SL, the band structure (more specifically, the band gap) of the AFM phase becomes very different from that of the FM phase. The band gap of AFM or Ferri-AFM decreases to tens or even several meV, which depends on defect details. However, the band gap of FM remains above 55 meV (summarized in Table I), which is less sensitive to the co-antisite density. All these different co-antisite configurations can arise randomly with varied densities in real materials. Thus, the experimental surface magnetic gap can be position and field dependent, i.e., the gap size depends on the magnetic field (which determines the magnetic configuration) and real space positions (which are related to different co-antisites) of measurements, as evidenced by recent scanning tunneling microscopy or spectroscopy experiments [67]. In ARPES, the overall surface magnetic gap can be reduced to the smallest one (or even smaller due to band misalignment) if different co-antisites coexist in the AFM or Ferri-AFM phase, rationalizing the diminishing gap in experiments.

TABLE I. Band gaps of $MnBi_2Te_4$ surfaces with different cation co-antisites under different magnetic configurations. The band gap is in units of millielectron volts (meV).

Surface	Cell-size	FM	AFM	Ferri-AFM
Perfect		69	60	
sNN	2 × 2	55	13	1
	3 × 3	72	6	4
	4 × 4	74	31	
sNNN	2 × 2	58	23	15
	3 × 3	73	18	20
	4 × 4	72	40	
bNN	2 × 2	66	43	50
	3 × 3	72	29	36
	4 × 4	65	22	
bNNN	2 × 2	76	21	40
	3 × 3	75	6	17
	4 × 4	65	24	

Band structures in Fig. 2 show that the topological surface states near the Γ point change in dispersion due to these co-antisites for both AFM and FM phases, especially the highest surface valence band (SVB) and lowest surface conduction band (SCB). The dispersion change originates in the charge redistribution of corresponding states. In Fig. 3, we plot the charge distribution of SVB and SCB at Γ and trace their evolution for the perfect surface and sNNN case as an example (situations are similar for other three defects [65]). On the perfect surface, charge densities of SVB and SCB under AFM are mainly concentrated on the top SL (notice the pronounced peak at the upper border) with limited distribution in the second SL. Charge densities of SVB and SCB are distributed in a relatively extended way under FM. When co-antisites appear, charge densities of both SVB and SCB are pushed toward the second SL under both AFM and FM (Centroids of the surface states move about 1–2 Å downward. Also notice the reduced peak at the upper border of the first SL.) Consequently, the top SL contribution to surface states is suppressed while the second SL contribution is enhanced. Similar charge redistribution caused by other factors such as surface charges and vdW gap expansion is also reported [35,36,59].

On the perfect surface, surface states are mainly distributed on the surface SL and the magnetism of the surface SL dominates the magnetic exchange interaction, opening the magnetic gap. Since the second SL is relatively far from surface states, its exchange interaction with surface states has a weaker effect on the magnetic gap. While the major exchange interaction of the surface SL explains the comparable magnetic gap between FM and AFM phases (69 vs 60 meV), the extra exchange interaction contribution of the second SL induces a slightly larger magnetic gap in the FM than in the AFM phase. On surfaces with co-antisites where surface charges are pushed toward the second SL, the top SL influence on the magnetic gap is reduced while the second SL influence is enhanced simultaneously. As illustrated in Fig. 4, the first and second SLs compete in exchange interaction with the topological surface states under AFM, leading to a suppressed

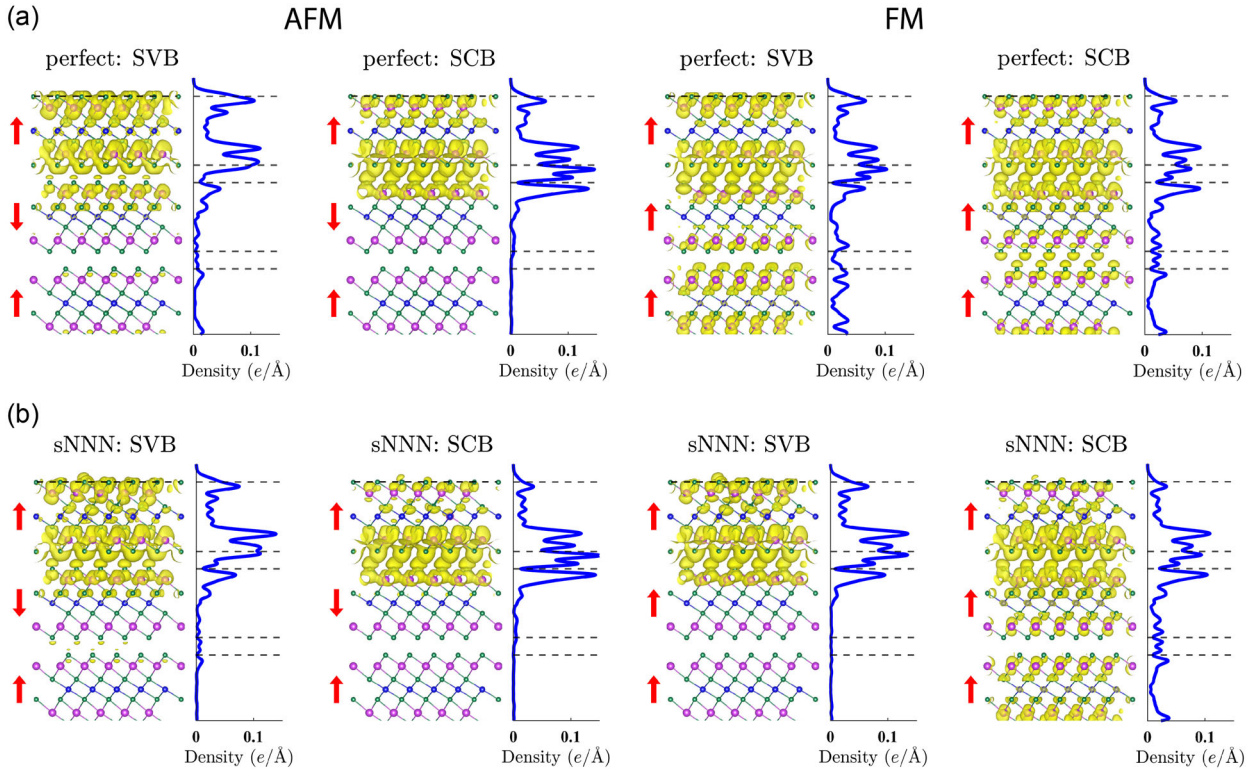

FIG. 3. Charge distribution of the top surface valence band (SVB) and bottom surface conduction band (SCB) at the Γ point of the perfect surface (a) and surface with sNNN co-antisites (b) (see the configuration in Fig. 1). Corresponding band structures under AFM and FM are shown in Fig. 2. The left part of each panel shows the charge distribution in the lattice (isosurface of 3.4×10^{-4} $e/\text{Å}^3$), and the right part shows the corresponding planar average along the out-of-plane direction [68]. The red vectors indicate the magnetic configuration in each SL. Only three SL layers are shown for simplicity, where the top dashed line of each panel indicates the surface. Compared to the perfect surface, the charge density of the sNNN surface is distributed closer to the vdW gap (the centroid of charge density is moved 1–2 Å toward the vdW gap).

magnetic gap for AFM. In contrast, the top two SLs exhibit the same magnetization in the FM phase and thus will not necessarily reduce the magnetic gap.

This mechanism is different from the previously proposed one [60] based on the magnetism cancellation by the

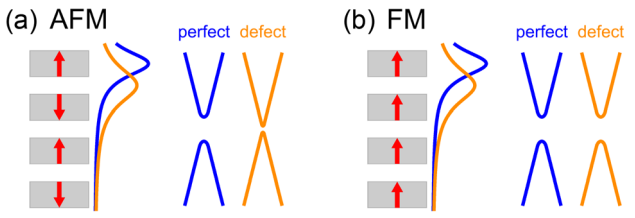

FIG. 4. Schematics for the relationship between surface charge distribution and magnetic gap under AFM (a) and FM (b). The red vectors represent the magnetic configuration. For a perfect surface where surface states (blue curves) are mainly distributed in the surface SL (gray rectangles), the topological surface states (blue linear crossing lines) under both AFM and FM open a magnetic gap. For a defective surface where surface states (orange curves) are pushed down toward the second SL, the magnetic gap is diminished heavily under AFM while not changing under FM (orange crossing lines).

antiparallel alignment of the Mn_{Bi} moment to other magnetic moments in the same SL. In our proposal, such an antiparallel alignment of Mn_{Bi} moment has a minor effect on the surface magnetic gap in $MnBi_2Te_4$. Instead, the magnetic exchange interaction of the second SL plays an essential role in determining the magnetic gaps of surfaces with defects.

Recent theoretical works [36,58] find that the magnetic gap can be reduced and even closed by the surface vdW gap expansion. At the same time, surface states are redistributed toward the second SL with its expansion [69]. We point out that such a gap reduction can also be explained by our theory. We also confirm that the magnetic gap of the FM phase is robust with the surface vdW gap expansion in $MnBi_2Te_4$ [65]. Thus, the cancellation of the magnetic exchange interaction by the second SL under AFM can be a generic mechanism of the reduced surface magnetic gap for various surface defects or disorders.

Discussions.—To realize topological surface states with a magnetic gap in $MnBi_2Te_4$, our work indicates practical strategies to optimize the material. One basic strategy is to improve the sample quality by reducing surface antisite defects. The basic idea behind this strategy is that

topological surface states should distribute mainly in the top SL. Thus one may alternatively bring the $MnBi_2Te_4$ surface close to another polar insulator, where the charge density of topological surface states can be attracted to the top SL by the modified surface potential [70]. This may be a promising way that requires further exploration in future work.

Another strategy is to realize intrinsic FM order in $MnBi_2Te_4$, where the surface magnetic gap may be more tolerant to the sample quality. In recent experiments, the FM phase was realized in superlattices $(MnBi_2Te_4)(Bi_2Te_3)_3$ [21,22,25] and Sb-doped $(MnBi_2Te_4)(Bi_2Te_3)$ [71,72]. As proposed in Ref. [71], the FM coupling between neighboring SLs is mediated by the AFM coupling between SLs and the Mn_{Bi} antisites in Bi_2Te_3 layers. But ARPES still observed gapless surface states in these FM samples. We point out that such Mn_{Bi} antisites in the Bi_2Te_3 layers may play the role of the second SL as in the AFM $MnBi_2Te_4$. Because they can cancel the exchange interaction of the surface SL, Mn_{Bi} antisites in the Bi_2Te_3 layer may be less helpful for the magnetic gap than expected. Besides, as we reported previously, such superlattices suffer from additional limitations (surface selection and film thickness) to ensure a surface band gap [73].

Conclusion.—We have studied the effect of co-antisites on the surface magnetic gap of $MnBi_2Te_4$ and found that the charge density of topological surface states is pushed toward the second van der Waals layer. The increased exchange interaction between topological surface states and the second SL layer decreases the surface magnetic gap for the AFM phase but affects little the gap for the FM phase. Our work reconciles contradicting observations between theory, ARPES and transport experiments and proposes material strategies to realize intriguing QAHE and AI in $MnBi_2Te_4$-family magnetic topological insulators.

We acknowledge helpful discussions with Igor Mazin and Chong Wang. B. Y. acknowledges the financial support from the European Research Council (ERC Consolidator Grant, No. 815869), and the Israel Science Foundation (ISF No. 3520/20).

[1] C.-Z. Chang *et al.*, Science **340**, 167 (2013).
[2] M. Mogi, M. Kawamura, A. Tsukazaki, R. Yoshimi, K. S. Takahashi, M. Kawasaki, and Y. Tokura, Sci. Adv. **3**, eaao1669 (2017).
[3] D. Xiao, J. Jiang, J.-H. Shin, W. Wang, F. Wang, Y.-F. Zhao, C. Liu, W. Wu, M. H. W. Chan, N. Samarth, and C.-Z. Chang, Phys. Rev. Lett. **120**, 056801 (2018).
[4] A. Sekine and K. Nomura, J. Appl. Phys. **129**, 141101 (2021).
[5] Y. Gong *et al.*, Chin. Phys. Lett. **36**, 076801 (2019).
[6] M. M. Otrokov *et al.*, Nature (London) **576**, 416 (2019).
[7] J. Li, Y. Li, S. Du, Z. Wang, B.-L. Gu, S.-C. Zhang, K. He, W. Duan, and Y. Xu, Sci. Adv. **5**, eaaw5685 (2019).
[8] D. Zhang, M. Shi, T. Zhu, D. Xing, H. Zhang, and J. Wang, Phys. Rev. Lett. **122**, 206401 (2019).
[9] Y. Deng, Y. Yu, M. Z. Shi, Z. Guo, Z. Xu, J. Wang, X. H. Chen, and Y. Zhang, Science **367**, 895 (2020).
[10] J. Ge, Y. Liu, J. Li, H. Li, T. Luo, Y. Wu, Y. Xu, and J. Wang, Natl. Sci. Rev. **7**, 1280 (2020).
[11] C. Liu, Y. Wang, H. Li, Y. Wu, Y. Li, J. Li, K. He, Y. Xu, J. Zhang, and Y. Wang, Nat. Mater. **19**, 522 (2020).
[12] H. Deng, Z. Chen, A. Wołoś, M. Konczykowski, K. Sobczak, J. Sitnicka, I. V. Fedorchenko, J. Borysiuk, T. Heider, Ł. Pluciński, K. Park, A. B. Georgescu, J. Cano, and L. Krusin-Elbaum, Nat. Phys. **17**, 36 (2021).
[13] J.-Q. Yan, ECS J. Solid State Sci. Technol. **11**, 063007 (2022).
[14] J. Wu, F. Liu, M. Sasase, K. Ienaga, Y. Obata, R. Yukawa, K. Horiba, H. Kumigashira, S. Okuma, T. Inoshita, and H. Hosono, Sci. Adv. **5**, eaax9989 (2019).
[15] S. H. Lee *et al.*, Phys. Rev. X **11**, 031032 (2021).
[16] C. Lei, S. Chen, and A. H. MacDonald, Proc. Natl. Acad. Sci. U.S.A. **117**, 27224 (2020).
[17] H. Li, C.-Z. Chen, H. Jiang, and X. C. Xie, Phys. Rev. Lett. **127**, 236402 (2021).
[18] P. Wang, J. Ge, J. Li, Y. Liu, Y. Xu, and J. Wang, The Innovation **2**, 100098 (2021).
[19] Y. Zhao and Q. Liu, Appl. Phys. Lett. **119**, 060502 (2021).
[20] Q. Li, C. X. Trang, W. Wu, J. Hwang, D. Cortie, N. Medhekar, S.-K. Mo, S. A. Yang, and M. T. Edmonds, Adv. Mater. **34**, 2107520 (2022).
[21] I. I. Klimovskikh *et al.*, npj Quantum Mater. **5**, 54 (2020).
[22] C. Hu *et al.*, Sci. Adv. **6**, eaba4275 (2020).
[23] J. Wu, F. Liu, C. Liu, Y. Wang, C. Li, Y. Lu, S. Matsuishi, and H. Hosono, Adv. Mater. **32**, 2001815 (2020).
[24] X. Wu *et al.*, Phys. Rev. X **10**, 031013 (2020).
[25] R. Lu *et al.*, Phys. Rev. X **11**, 011039 (2021).
[26] R. C. Vidal *et al.*, Phys. Rev. X **9**, 041065 (2019).
[27] N. H. Jo, L.-L. Wang, R.-J. Slager, J. Yan, Y. Wu, K. Lee, B. Schrunk, A. Vishwanath, and A. Kaminski, Phys. Rev. B **102**, 045130 (2020).
[28] C. Hu, K. N. Gordon, P. Liu, J. Liu, X. Zhou, P. Hao, D. Narayan, E. Emmanouilidou, H. Sun, Y. Liu, H. Brawer, A. P. Ramirez, L. Ding, H. Cao, Q. Liu, D. Dessau, and N. Ni, Nat. Commun. **11**, 97 (2020).
[29] R. C. Vidal, H. Bentmann, J. I. Facio, T. Heider, P. Kagerer, C. I. Fornari, T. R. F. Peixoto, T. Figgemeier, S. Jung, C. Cacho, B. Büchner, J. van den Brink, C. M. Schneider, L. Plucinski, E. F. Schwier, K. Shimada, M. Richter, A. Isaeva, and F. Reinert, Phys. Rev. Lett. **126**, 176403 (2021).
[30] M. M. Otrokov, I. P. Rusinov, M. Blanco-Rey, M. Hoffmann, A. Y. Vyazovskaya, S. V. Eremeev, A. Ernst, P. M. Echenique, A. Arnau, and E. V. Chulkov, Phys. Rev. Lett. **122**, 107202 (2019).
[31] S. Tian, S. Gao, S. Nie, Y. Qian, C. Gong, Y. Fu, H. Li, W. Fan, P. Zhang, T. Kondo, S. Shin, J. Adell, H. Fedderwitz, H. Ding, Z. Wang, T. Qian, and H. Lei, Phys. Rev. B **102**, 035144 (2020).
[32] X.-M. Ma, Z. Chen, E. F. Schwier, Y. Zhang, Y.-J. Hao, S. Kumar, R. Lu *et al.*, Phys. Rev. B **102**, 245136 (2020).
[33] H. Zhong, C. Bao, H. Wang, J. Li, Z. Yin, Y. Xu, W. Duan, T.-L. Xia, and S. Zhou, Nano Lett. **21**, 6080 (2021).
[34] S. H. Lee, Y. Zhu, Y. Wang, L. Miao, T. Pillsbury, H. Yi, S. Kempinger, J. Hu, C. A. Heikes, P. Quarterman, W. Ratcliff,

J. A. Borchers, H. Zhang, X. Ke, D. Graf, N. Alem, C.-Z. Chang, N. Samarth, and Z. Mao, Phys. Rev. Res. **1**, 012011 (2019).
[35] A. M. Shikin, D. A. Estyunin, N. L. Zaitsev, D. Glazkova, I. I. Klimovskikh *et al.*, Phys. Rev. B **104**, 115168 (2021).
[36] A. M. Shikin, D. Estyunin, I. I. Klimovskikh, S. Filnov, E. Schwier, S. Kumar, K. Miyamoto, T. Okuda, A. Kimura, K. Kuroda *et al.*, Sci. Rep. **10**, 13226 (2020).
[37] H.-R. Ji, Y.-Z. Liu, H. Wang, J.-W. Luo, J.-H. Li, H. Li, Y. Wu, Y. Xu, and J. Wang, Chin. Phys. Lett. **38**, 107404 (2021).
[38] Y.-J. Hao *et al.*, Phys. Rev. X **9**, 041038 (2019).
[39] H. Li *et al.*, Phys. Rev. X **9**, 041039 (2019).
[40] Y. J. Chen *et al.*, Phys. Rev. X **9**, 041040 (2019).
[41] P. Swatek, Y. Wu, L.-L. Wang, K. Lee, B. Schrunk, J. Yan, and A. Kaminski, Phys. Rev. B **101**, 161109(R) (2020).
[42] L. Xu *et al.*, Sci. bull. **65**, 2086 (2020).
[43] Y. Hu, L. Xu, M. Shi, A. Luo, S. Peng, Z. Y. Wang, J. J. Ying, T. Wu, Z. K. Liu, C. F. Zhang, Y. L. Chen, G. Xu, X.-H. Chen, and J.-F. He, Phys. Rev. B **101**, 161113(R) (2020).
[44] P. M. Sass, J. Kim, D. Vanderbilt, J. Yan, and W. Wu, Phys. Rev. Lett. **125**, 037201 (2020).
[45] D. Nevola, H. X. Li, J.-Q. Yan, R. G. Moore, H.-N. Lee, H. Miao, and P. D. Johnson, Phys. Rev. Lett. **125**, 117205 (2020).
[46] S. H. Lee, Y. Zhu, Y. Wang, L. Miao, T. Pillsbury, H. Yi, S. Kempinger, J. Hu, C. A. Heikes, P. Quarterman, W. Ratcliff, J. A. Borchers, H. Zhang, X. Ke, D. Graf, N. Alem, C.-Z. Chang, N. Samarth, and Z. Mao, Phys. Rev. Res. **1**, 012011 (R) (2019).
[47] D. Ovchinnikov, X. Huang, Z. Lin, Z. Fei, J. Cai, T. Song, M. He, Q. Jiang, C. Wang, H. Li, Y. Wang, Y. Wu, D. Xiao, J.-H. Chu, J. Yan, C.-Z. Chang, Y.-T. Cui, and X. Xu, Nano Lett. **21**, 2544 (2021).
[48] C. Liu, Y. Wang, M. Yang, J. Mao, H. Li, Y. Li, J. Li, H. Zhu, J. Wang, L. Li, Y. Wu, Y. Xu, J. Zhang, and Y. Wang, Nat. Commun. **12**, 4647 (2021).
[49] Z. Ying, S. Zhang, B. Chen, B. Jia, F. Fei, M. Zhang, H. Zhang, X. Wang, and F. Song, Phys. Rev. B **105**, 085412 (2022).
[50] J. Cai, D. Ovchinnikov, Z. Fei, M. He, T. Song, Z. Lin, C. Wang, D. Cobden, J.-H. Chu, Y.-T. Cui *et al.*, Nat. Commun. **13**, 1668 (2022).
[51] T. Murakami, Y. Nambu, T. Koretsune, G. Xiangyu, T. Yamamoto, C. M. Brown, and H. Kageyama, Phys. Rev. B **100**, 195103 (2019).
[52] Y. Liu, L.-L. Wang, Q. Zheng, Z. Huang, X. Wang, M. Chi, Y. Wu, B. C. Chakoumakos, M. A. McGuire, B. C. Sales, W. Wu, and J. Yan, Phys. Rev. X **11**, 021033 (2021).
[53] Y. Lai, L. Ke, J. Yan, R. D. McDonald, and R. J. McQueeney, Phys. Rev. B **103**, 184429 (2021).
[54] Z. Huang, M.-H. Du, J. Yan, and W. Wu, Phys. Rev. Mater. **4**, 121202(R) (2020).
[55] F. Hou, Q. Yao, C.-S. Zhou, X.-M. Ma, M. Han, Y.-J. Hao, X. Wu, Y. Zhang, H. Sun, C. Liu, Y. Zhao, Q. Liu, and J. Lin, ACS Nano **14**, 11262 (2020).
[56] Y. Yuan, X. Wang, H. Li, J. Li, Y. Ji, Z. Hao, Y. Wu, K. He, Y. Wang, Y. Xu, W. Duan, W. Li, and Q.-K. Xue, Nano Lett. **20**, 3271 (2020).
[57] H.-P. Sun, C. M. Wang, S.-B. Zhang, R. Chen, Y. Zhao, C. Liu, Q. Liu, C. Chen, H.-Z. Lu, and X. C. Xie, Phys. Rev. B **102**, 241406(R) (2020).
[58] D. Wang, H. Wang, D. Xing, and H. Zhang, arXiv:2205.08204.
[59] A. M. Shikin, T. P. Makarova, A. V. Eryzhenkov, D. Y. Usachov, D. A. Estyunin, D. A. Glazkova, I. I. Klimovskikh, A. G. Rybkin, and A. V. Tarasov, arXiv:2205.07501.
[60] M. Garnica, M. Otrokov, P. C. Aguilar, I. Klimovskikh, D. Estyunin, Z. Aliev, I. Amiraslanov, N. Abdullayev, V. Zverev, M. Babanly *et al.*, npj Quantum Mater. **7**, 7 (2022).
[61] S. Wimmer *et al.*, Adv. Mater. **33**, 2102935 (2021).
[62] G. Kresse and J. Furthmüller, Comput. Mater. Sci. **6**, 15 (1996).
[63] G. Kresse and J. Furthmüller, Phys. Rev. B **54**, 11169 (1996).
[64] J. P. Perdew, K. Burke, and M. Ernzerhof, Phys. Rev. Lett. **77**, 3865 (1996).
[65] See Supplemental Material at http://link.aps.org/supplemental/10.1103/PhysRevLett.130.126702 for magnetic configurations as well as total energies of different surfaces, band structures of $MnBi_2Te_4$ surfaces with different single antisites, two antisites in two SLs, and co-antisites in the surface SL under different densities, charge distributions of SVB and SCB of defects not shown in the main text, band structure evolution of $MnBi_2Te_4$ with surface vdW gap expansion (under AFM and FM), as well as band structures of $MnBi_2Te_4$-terminations with different co-antisites in $MnBi_4Te_7$ and $MnBi_6Te_{10}$.
[66] M.-H. Du, J. Yan, V. R. Cooper, and M. Eisenbach, Adv. Funct. Mater. **31**, 2006516 (2021).
[67] M. Liu, C. Lei, H. Kim, Y. Li, L. Frammolino, J. Yan, A. H. Macdonald, and C.-K. Shih, Proc. Natl. Acad. Sci. U.S.A. **119**, e2207681119 (2022).
[68] For the perfect surface under AFM, the charge density of SVB (SCB) is distributed in two bands with nearly the same energies. Thus the charge densities of the two bands are added up for SVB (SCB) charge densities of the perfect surface under AFM. For the perfect surface under FM, since topological surface states are distributed in two lowest conduction bands, their respective charge densities are also added up for the SVB/SCB. Similar treatment is applied for the SCB of a defective surface under FM.
[69] S. V. Eremeev, M. G. Vergniory, T. V. Menshchikova, A. A. Shaposhnikov, and E. V. Chulkov, New J. Phys. **14**, 113030 (2012).
[70] V. N. Menshov, V. V. Tugushev, and E. V. Chulkov, JETP Lett. **104**, 453 (2016).
[71] C. Hu, S.-W. Lien, E. Feng, S. Mackey, H.-J. Tien, I. I. Mazin, H. Cao, T.-R. Chang, and N. Ni, Phys. Rev. B **104**, 054422 (2021).
[72] Y. D. Guan, C. H. Yan, S. H. Lee, X. Gui, W. Ning, J. L. Ning, Y. L. Zhu, M. Kothakonda, C. Q. Xu, X. L. Ke, J. W. Sun, W. W. Xie, S. L. Yang, and Z. Q. Mao, Phys. Rev. Mater. **6**, 054203 (2022).
[73] H. Tan and B. Yan, Phys. Rev. B **105**, 165130 (2022).